The grain size distribution of matrix in primitive chondrites

E. VACCARO [1]*, P. WOZNIAKIEWICZ[2], I. A. FRANCHI [3], N. STARKEY[3], and
S. S. RUSSELL [1,3]

[1]Mineral and Planetary Sciences Division, The Natural History Museum, London, UK
[2]School of Physical Sciences, University of Kent, Canterbury, UK
[3]Planetary & Space Sciences, Open University, Milton Keynes, UK
*Corresponding author.
E. Vaccaro, Mineral and Planetary Sciences Division, The Natural History Museum, London, UK.
E-mail: e.vaccaro@nhm.ac.uk

Abstract–The matrix of primitive chondrites is composed of submicron crystals embedded in amorphous silicates. These grains are thought to be the remains of relatively unprocessed dust from the inner regions of the protoplanetary disk. The matrix of primitive meteorites is often compared to chondritic porous interplanetary dust particles (CP-IDPs) which are believed to be of cometary origin, having accreted in the outermost regions of the solar nebula. Crystalline grains in CP-IDPs show evidence of a size–density relationship between the silicates and sulfides suggesting that these components experienced sorting prior to accretion. Here, we investigate whether such evidence of sorting is also present in the matrix constituents of primitive chondrites. We report findings from our study of grain size distributions of discrete silicate and opaque (sulfide and metal) grains within the matrix of the primitive meteorites Acfer 094 (C2-ung.), ALHA77307 (CO3), MIL 07687 (C3-ung.), and QUE 99177 (CR2). Mean radii of matrix silicate grains range from 103 nm in QUE 99177 to 2018 nm in MIL 07687. The opaque grains show a wider variation, with average radii ranging from 15 nm in QUE 99177 to 219 nm in MIL07687. Our results indicate that, in contrast to CP-IDPs, the size distribution of matrix components of these primitive meteorites cannot be explained by aerodynamic sorting that took place prior to accretion. We conclude that any evidence of sorting is likely to have been lost due to a greater variety and degree of processing experienced on these primitive chondrites than on cometary parent bodies.

INTRODUCTION

Since the turn of the century, a new generation of telescopes has been providing the opportunity to study the grains that populate protoplanetary disks around pre-main sequence stars. These studies have identified crystalline silicates (olivines and pyroxenes) in the warm inner disk regions (Watson et al., 2009) with more recent observations suggesting these grains can be entrained in protostellar outflows and then rained down on the protostar and disk (Poteet et al., 2011). Other observations also show that there are variations in the size distribution of crystalline grains within these disks, and in particular, a reduction in size with distance from the star (Van Boekel et al., 2004). The dynamics of

protoplanetary dust grains are driven by disk winds and magneto-rotational turbulence causing small dust grains, which are strongly coupled to the gas, to be dragged upward with the upflowing gas while large grains remain near the mid-plane of a disk (Miyake et al., 2016). In order to investigate and understand the disk processes that have shaped our own solar system, we must study samples that have remained minimally altered since accretion. For the outer regions, such primitive samples may be found in comets, while evidence of processes in the inner regions may be found in primitive asteroids.

Cometary samples have been returned to the Earth by NASA's Stardust mission for analyses and are also thought to be represented in interplanetary dust particles (IDP) collected in the Earth's atmosphere in the form of

the chondritic porous (CP) IDPs. CP IDPs exhibit a porous, fragile structure which is consistent with the brittle nature of cometary meteors inferred from observations of their disaggregation during atmospheric entry (Verniani, 1969). They are also characterized by a high abundance of isotopically anomalous presolar grains, high carbon content, and anhydrous mineralogy all suggesting that they originated from small, frozen parent bodies in the outer solar system (Bradley, 2013; Busemann et al., 2009; Davidson et al., 2012; Messenger, 2000; Nguyen et al., 2007). Their ~10 µm infrared silicate features are also similar to those observed in the astronomical spectra of comets (Bradley, 1999; Molster & Waters, 2003; Sandford & Walker, 1985). Furthermore, the atmospheric entry velocity of some CP IDPs is consistent with that of cometary orbits (Brownlee et al., 1993; Brownlee & Joswiak, 1995). These characteristics, all suggest that they accreted in the outermost regions of the solar nebula as comets.

Chondrites are thought to originate from unmelted asteroids. These have undergone varying degrees of parent body processing, as indicated by their petrological type, with type 3 being the least altered, types 1 and 2 representing samples that have experienced aqueous alteration on the parent body, and types 4–6 exhibiting evidence of thermal alteration. These meteorites are thought to preserve remnants from the disk stage of solar system evolution. The presence of amorphous silicates within the matrix of primitive chondrites has been thought to indicate that the matrix has experienced only limited alteration (e.g., Hopp & Vollmer, 2018; Le Guillou et al., 2015; Ohtaki et al., 2021; Vollmer et al., 2020) and has not experienced significant thermal metamorphism, as even a small increase of temperature would have converted the amorphous silicates into crystalline mineralogical phases (e.g., Brearley, 1993). The possibility of one or more asteroidal processes that could have operated on the meteorite matrix materials, based on our findings, is discussed further in Discussion section.

Studies of the size distributions of magnesium-rich silicate chondrules and calcium-, aluminum-rich refractory inclusions (CAIs) have shown a remarkable similarity within various subgroups of chondritic components implying a common size sorting process (Simon et al., 2018; Teitler et al., 2010). While chondrule sizes vary widely between groups, for example, COs have much smaller chondrules than CVs and CRs, for each individual group, the shape of the size distributions is similar when normalized to their modal value (Simon et al., 2018; Teitler et al., 2010). This is consistent with the findings of Wozniakiewicz et al. (2012, 2013) where particle sizes may vary from one IDP to another, but particles of different density are sorted together, with the same density ratio.

This first led to a model of chondrite parent body formation mechanism that involved size sorting by aerodynamic particle–gas interactions (e.g., Cuzzi et al., 2008; Hartlep & Cuzzi, 2020; Metzel et al., 2019; Rubin & Keil, 1984; Skinner & Leenhouts, 1993; Teitler et al., 2010).

Investigations of crystalline grain size distributions in CP-IDPs and Stardust samples suggest evidence of pre-accretional processes that are preserved in cometary samples (Wozniakiewicz et al., 2012, 2013). In that work, a size–density relationship was identified between the crystalline silicates and sulfides suggesting that the particles experienced sorting prior to accretion. Similar investigations into the size distributions for chondrules and large opaque phases in ordinary chondrites have also been conducted. These studies have found these larger constituents have the same mean size–density product, believed to be a consequence of a sorting mechanism that took place prior to accretion (Kuebler et al., 1999).

The gas dynamics model proposed by Clayton (1980) is one of several natural processes evoked to explain the aerodynamic sorting of the large grains in chondritic meteorites. According to this model, particles traveling in a medium of gas experience a force resisting the relative motion of the solid surface, which reduces their speed as they penetrate the medium. This resisting force and the consequential slowing depend on the size and density of the particles. Therefore, chondritic meteorite constituents moving in a turbulent medium, coupling to the gas due to the particle's density, settle at different speeds. Turbulence in the disk could also be responsible for size sorting into aggregates of a certain size–density, or concentration and segregation into different volumes (Cuzzi et al., 2001). Small grains are thought to form aggregates everywhere, which can be swept up onto the surface of microscopic particles like chondrules (e.g., Cuzzi et al., 2017; Hartlep et al., 2017); however, the gas density in the asteroid-forming region may be too large to allow the matrix-sized "grains" to have size-dependent relative velocities and sticking properties, as apparently observed for grains in cometary aggregates by Wozniakiewicz et al. (2012, 2013). In this scenario, it is the chondrule-sized particles in the asteroid-forming region that may grow into cm-sized aggregates and thus exhibit evidence of the size sorting signature observed in CP-IDPs.

These chondritic constituents then could have been accreted in rocky bodies in the asteroid belt region of the protoplanetary disk, between 2 and 4 AU, or in the outer solar system, preserving the sorting that is observed in the chondritic meteorites.

Shu et al. (1997) proposed another mechanism of aerodynamic sorting activated by the bipolar outflows, where grains settle onto the accretionary disk after being transported in a medium having negligible opposition to the flow above the plane of the protoplanetary disk.
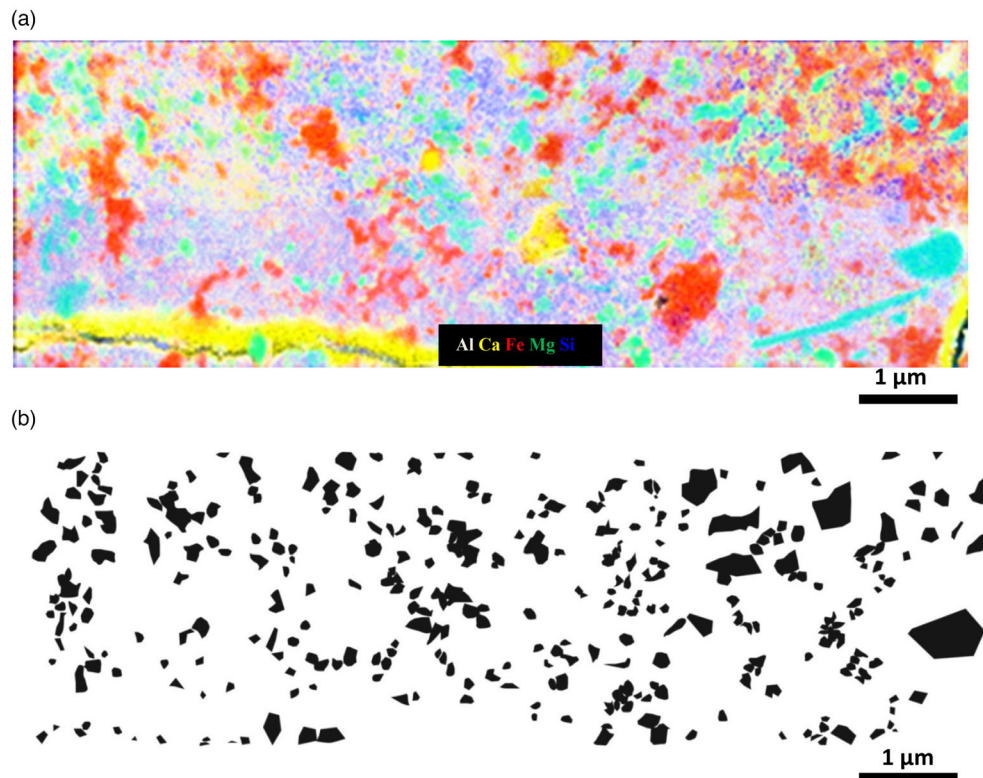
(a)

Al Ca Fe Mg Si

1 μm

(b)

1 μm

FIGURE 1. (a) Element map of ALHA77307 Area 1 acquired with FEI Quanta SEM. Al = white, Ca = yellow, Fe = red, Mg = green, Si = blue. The map shows the Fe-rich composition of the pale gray alteration phase, like that shown in Figure 8 (in red in this map), Mg-rich silicates (in green) set in an Si- and Fe-rich groundmass (in purple). The yellow feature at the bottom, occurring along the crack in the sample, is an SEM artifact. The highly elongated whisker-like grain in the lower right was not included in the data set, hence, not seen in (b). (b) Same field of view as 1a, with shapes traced around silicate phases (green and blue), determined by element map, in sample ALHA77307 matrix area. Polygons were traced by hand using Photoshop while comparing the secondary electron (SE) images acquired with the FEI Quanta 650 FEG SEM, and energy-selective backscattered detector (EsB) montages acquired using the Zeiss Ultra Plus Field Emission SEM.

Smaller and/or less dense grains settle at larger heliocentric distances (Liffman, 2005).

In these aerodynamic sorting models, grains as small as are found in CP IDPs would have been tightly coupled to the gas, prohibiting sorting by such mechanisms, yet sorting remains evident. Since CP IDPs share similarities with the matrix of primitive meteorites, evidence of sorting may also be preserved in the primitive chondrite matrix constituents if the process responsible operates over the entire disk. Alternatively, these grains may not show sorting if other nebular or parent body processes have obliterated these effects causing grains to either grow or be reduced in size or even totally destroyed. In order to investigate this, we measured discrete grains, characterized by a clear boundary/shape and readily visible on element maps and combined SE-element maps, of different phases (silicate vs. opaque sulfides and metal grains) within the matrix of four primitive meteorites: Acfer 094 (C2-ung.), ALHA77307 (CO3), MIL 07687 (C3-ung.), and QUE 99177 (CR2). Here, we describe the

abundances and the size distributions observed and discuss their implications.

METHODS

Element maps of each entire sample (standard petrographic thin sections, 30 μm thick, polished, and carbon coated) were first made, using the Zeiss EVO 15LS SEM at a spatial resolution of 3 μm. Regions of matrix approximately $25 \times 10 \, \mu m^2$ and that were not obviously affected by asteroidal or terrestrial weathering were selected (e.g., not showing extensive oxidation of metal grains). An FEI Quanta 650 FEG SEM was then used to obtain high-resolution element maps with spatial resolution of 10 nm, at an accelerating voltage of 6.00 kV of the matrix regions for the major elements (Al, Ca, Fe, Mg, Si).

Silicate grain sizes were measured using these element maps as follows. Combined element maps were imported into Photoshop© and used as a base to trace around the crystalline silicates (which appear green and blue in
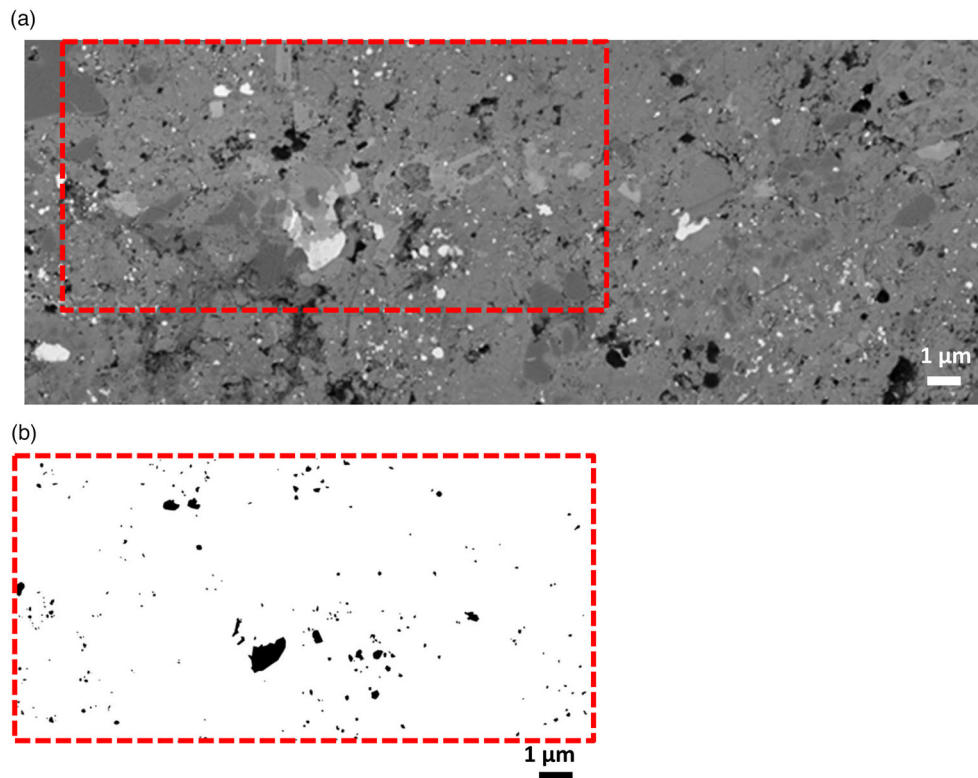
FIGURE 2. (a) Backscattered electron image of sample QUE 99177 Area 2 acquired using the Zeiss Ultra Plus SEM, at spatial resolution of 8 nm. (b) Traced shapes around opaque phases thresholded within the area of interest indicated by the red box in (a).

Figure 1). Comparison with secondary electron (SE) images acquired with the same instrument, and energy-selective backscattered detector (EsB) montages acquired using the Zeiss Ultra Plus Field Emission SEM helped to discriminate between a single grain and a group of grains. The surface areas (A) in μm^2 of the shapes traced around the silicates on the element maps acquired with the FEI Quanta 650 FEG SEM were calculated using Image J (Figure 1b). Approximating the grains as spherical, the radii (r) of the silicate crystals were calculated using the following formula: $r = (A/\pi)^{1/2}$. The smallest silicate grain measured with this method was reported in sample QUE99177 with a radius of 25 nm. Since the grain population was largely represented by rounded crystals, approximating them as spherical is thought to have a negligible impact on the results. We found two grains that were highly elongated (whisker shape) in all of our areas studied; these were not included in the data set.

When comparing element maps against the BSE images, it became apparent that an alternative method for measuring sulfides was required: The sulfides present within the samples were often much smaller than the silicates such that they were not always identified as individual grains in the element maps, and it was impossible to accurately trace an outline by hand for measurement. High spatial resolution EsB images of matrix regions of interest were therefore acquired using the Zeiss Ultra Plus Field Emission SEM.

In order to obtain image montages of matrix regions at a spatial resolution of 8 nm, images were acquired at a low accelerating voltage of 3.00 kV and ~2.5 mm working distance (WD). Using different images with comparable spatial resolution to trace silicates (10 nm) and opaques (8 nm) is thought to introduce minimal bias in the results. However, there is a potential source of error due to human eye and tracing by hand (resulting in an estimated 5%–10% error in the final radius, with a larger error for smaller grains), and due to smaller grains (less than 10 nm) embedded to groundmass not visible with the SEM.

These operating conditions, ideal for high spatial resolution imaging, do not allow for the acquisition of compositional (multiple band) data; therefore, our interpretation of the mineralogy is based on apparent brightness (corresponding to atomic density) in the image montages alone. The brighter phases in the EsB image contain high atomic number elements and these are typically metal and metal–sulfide phases as confirmed by EDX investigations. On this basis, it is not possible to discern metal grains from iron–sulfides, and we thus
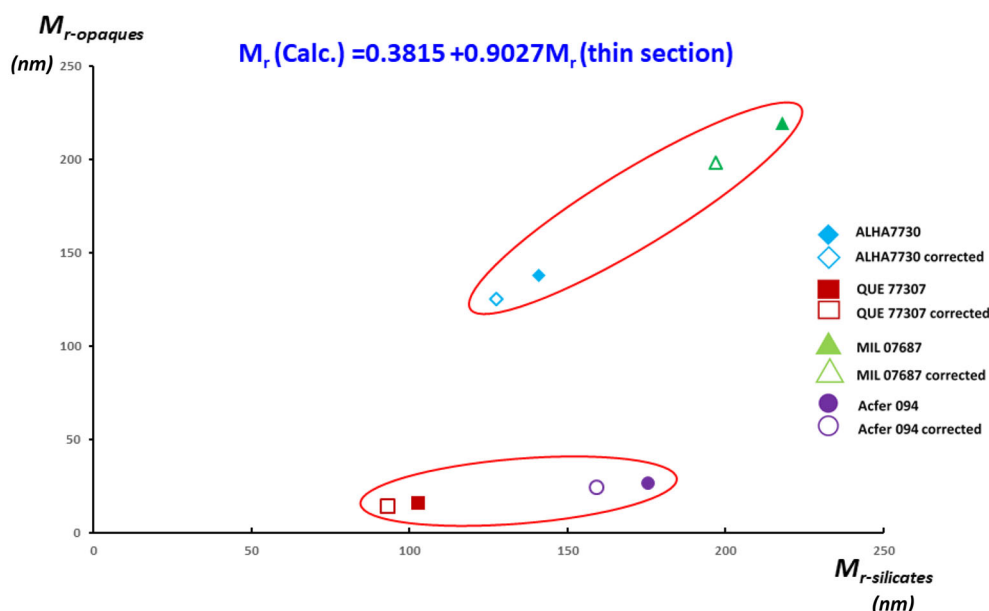
FIGURE 3. Diagram showing geometric mean radii of opaques ($M_{r\text{-opaques}}$) in nanometers versus geometric mean radii of silicates ($M_{r\text{-silicates}}$) in nanometers to consider the potential effects of sectioning bias due to the measurement in 2D. Plotted are uncorrected values obtained from five areas on each of the four samples (solid symbols) and corrected values (open symbols).

classify bright phases as simply opaque phases. This ambiguity will be discussed below.

To improve accuracy, the intensity histogram of the image was used to determine the correct segmentation by isolating the region of the histogram that corresponded to the bright phases (falling in the range between the values 255 and 165 in a scale between 0 and 255). The thresholded image that relates to the opaque phases was then used as a base for tracing grain outlines. The thresholding process is not considered to be a significant source of bias.

The areas and radii of the opaque phases in these images were then calculated following the method described above for silicates (Figure 2b) with the smallest opaque grain measured in sample QUE99177 having a radius of 2.25 nm. The opaque phases did not show evidence of compositional gradation or zonation within phases. Therefore, no bias is thought to affect the results due to the technique used.

Cumulative Frequencies, Geometric Mean, and Standard Deviations

In order to quantify and compare size distributions between silicate and Fe-rich-sulfide grain populations in cometary samples, Wozniakiewicz et al. (2012) found that the data sets were best described by log-normal distributions and thus determined the geometric mean and standard deviation for each. To enable a direct comparison to be made with the IDP work of Wozniakiewicz et al. (2012), a similar approach was applied to the
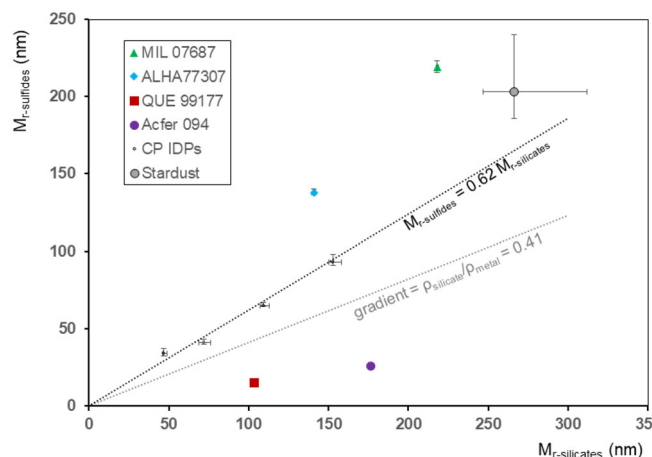

FIGURE 4. Geometric mean radii of opaques ($M_{r\text{-opaques}}$) versus geometric mean radii of silicates ($M_{r\text{-silicates}}$) all in nm, showing meteorite matrix data compared with that from CP-IDPs and Stardust grains (solid black round symbols) reported from Wozniakiewicz et al. (2012, 2013). Unlike the Wozniakiewicz 2012 and 2013 studies, where only data for Fe-rich sulfides were plotted against that of silicates, the opaque phases in this study may be metal, or a mixture of metal and metal–sulfides such as pyrrhotite, troilite, or pentlandite. Consequently, the gray trend line represents a slope of 0.41 (an approximate ratio of silicate to metal densities) for comparison. Error bars representing standard error on the mean are hidden in some cases for the meteorites by the size of the icons used.

meteorite matrix grain size data reported in this study. The cumulative frequency of the grains' radii was plotted against the natural log of the radius and the geometric
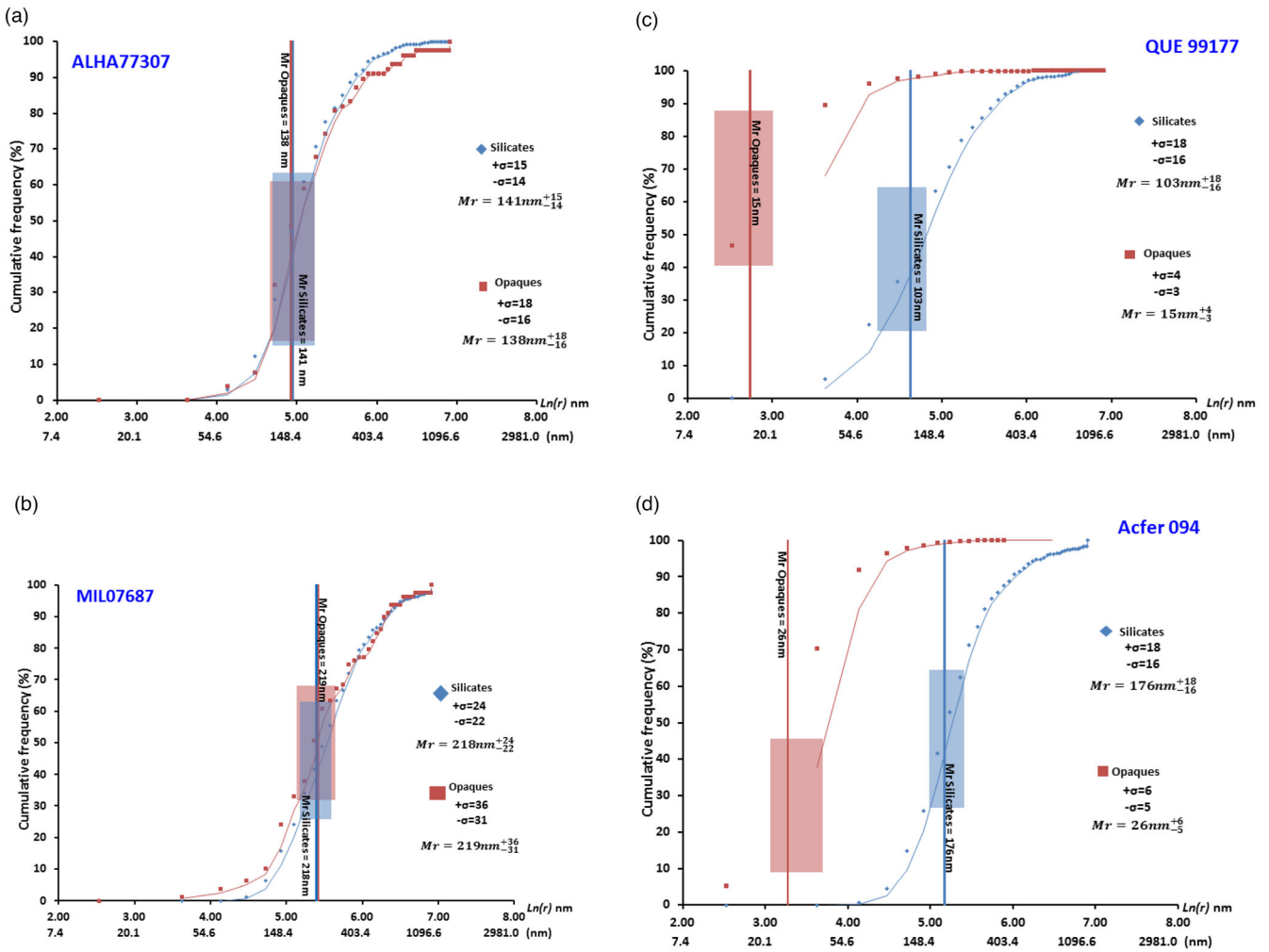
FIGURE 5. Cumulative frequency curves plotted as a function of ln(r) and fitted with a moving average of sample ALHA77307 (a), MIL 07687 (b), QUE 99177 (c), Acfer 094 (d) using the modified geometric Folk and Ward (1957) equations of Blott and Pye.

mean radii (Mr in nm) and standard deviations (+σ and −σ in nm) were calculated graphically using the modified geometric Folk and Ward (1957) equations of Blott and Pye (2001) below:

$$M_r = \exp\left[\frac{\ln P_{16} + \ln P_{50} + \ln P_{84}}{3}\right] \quad (1)$$

$$+\sigma = \exp\left[\ln M_r + \left(\frac{\ln P_{84} - \ln P_{16}}{4} + \frac{\ln P_{95} - \ln P_5}{6.6}\right)\right] - M_r \quad (2)$$

$$-\sigma = M_r - \exp\left[\ln M_r - \left(\frac{\ln P_{84} - \ln P_{16}}{4} + \frac{\ln P_{95} - \ln P_5}{6.6}\right)\right]. \quad (3)$$

The values of P_5, P_{16}, P_{50}, P_{84}, and P_{95} are the grain sizes referring to the 5th, 16th, 50th, 84th, and 95th percentiles, respectively. The original geometric Folk and Ward (1957) equations were expressed logarithmically (in φ units) where phi (φ) values were φ = −log 2d, and d is the grain diameter in millimeters, a unit commonly employed in the field of sedimentology. Blott and Pye (2001) preferred statistics to be expressed geometrically (in metric units), and used Equations (1–3) to convert geometric mean and the standard deviation in nm units. The graphical method is commonly used in sedimentology and has also been applied previously to extraterrestrial samples (e.g., chondrule measurements by Kuebler et al., 1999).

2-D–3-D Correction

The grain sizes measured in the four (2-D) thin sections and their distribution of observed random grain diameters might not be a true reflection of whole grains in the 3-D, uncut, and unpolished sample. Friedman (1958)

TABLE 1. Geometric mean radii (M_r), standard deviation values on the mean ($+\sigma$, $-\sigma$) for silicates and opaque phases for samples Allan Hills A77307 (ALHA77307), Miller Range 07687 (MIL 07687), Queen Alexander Range 99,177 (QUE 99177), and Acfer 094.

Allan Hills A77307	Silicates	Opaques	Miller Range 07687	Silicates	Opaques
P95 (ln)	5.82	6.03	P95 (ln)	6.42	6.4
P84 (ln)	5.47	5.55	P84 (ln)	5.93	6.29
P50 (ln)	4.92	4.9	P50 (ln)	5.41	5.26
P16 (ln)	4.45	4.34	P16 (ln)	4.82	4.63
P5 (ln)	4.16	4.05	P5 (ln)	4.54	3.86
Mr (nm)	141	138	Mr (nm)	218	219
($+\sigma$)	15	18	($+\sigma$)	24	36
($-\sigma$)	14	16	($-\sigma$)	22	31
Number of particles measured	709	78	Number of particles measured	662	79
Queen Alexander Range 99177	Silicates	Opaques	Acfer 094	Silicates	Opaques
P95 (ln)	5.83	4.06	P95 (ln)	6.14	4.41
P84 (ln)	5.36	3.43	P84 (ln)	5.66	3.91
P50 (ln)	4.67	2.54	P50 (ln)	5.14	3.25
P16 (ln)	3.86	2.23	P16 (ln)	4.71	2.65
P5 (ln)	3.36	2.11	P5 (ln)	4.37	2.38
Mr (nm)	103	15	Mr (nm)	176	26
($+\sigma$)	18	4	($+\sigma$)	18	6
($-\sigma$)	16	3	($-\sigma$)	16	5
Number of particles measured	647	968	Number of particles measured	840	5007

Note: The values of P_5, P_{16}, P_{50}, P_{84}, and P_{95} are the natural logarithm of the grain sizes in nanometers, referring to the 5th, 16th, 50th, 84th, and 95th percentiles, respectively.

determined that a fixed relationship existed between sieved (3-D) and thin-section (2-D) grain size parameters and has expressed this relationship graphically. A correlation between sieved and thin-section grain sizes was established to enable the derivation of a sieved sample cumulative frequency curve from thin-section data. From this, a relation between the geometric mean radii of sieved ($M_{\text{r-sieved}}$) and sectioned ($M_{\text{r-thin-section}}$) samples can be expressed as follows:

$$M_{\text{r-sieved}} = 0.3815 + 0.9027 M_{\text{r-thin-section}}. \quad (4)$$

We have applied Equation (4) to our data to calculate the 3-D corrected value for M_r. Both corrected and uncorrected values have been plotted for opaque ($M_{\text{r-opaques}}$) and silicate ($M_{\text{r-silicates}}$) grains in Figure 3. When applied, the correction decreases the value of $M_{\text{r-silicates}}$ by <12% and $M_{\text{r-opaques}}$ in by <10% all samples. Both before and after the correction, the samples continue to occupy the same distinct regions of the plot, and thus, we deem this correction to have not significantly affected the results.

It is important to note here that Friedman's equation was determined for grain sizes several orders of magnitude larger than the size of the matrix grains in our samples (and several orders of magnitude larger than the topographical variation over a typical thin section). Given that the individual crystalline grains within our meteorite matrices are typically <1 μm, it is unlikely that they are sectioned during the sample preparation and instead, that the full 3-D nature of these small grains is revealed within the limited topography of the section. Given the uncertainty over the validity of applying the correction to such samples, and the apparent minor changes it causes to the results, we have chosen to use the original uncorrected values of M_r during the rest of our analyses.

RESULTS

For ALHA77307 and MIL 07687, a total of 709 and 662 silicate grains were measured, respectively, and the silicate grains in the matrix were similar in average size to the opaque grains, where the number of grains measured was 78 for ALHA77307 and 79 MIL 07687. We found that for ALHA77307, the geometric mean radii of silicates and opaques were 141 nm ($+\sigma15$, $-\sigma14$) and 138 nm ($+\sigma18$, $-\sigma16$), respectively. For MIL 07687, the grains were on average coarser, with the mean radii of 218 nm ($+\sigma24$, $-\sigma22$) for silicates and 219 nm ($+\sigma36$, $-\sigma31$) for opaques. For the other two meteorites in our study, a total of 647 silicate grains in QUE 99177 and 840 in Acfer 094 were measured, and for the opaques, these values were 968 and 5007, respectively.
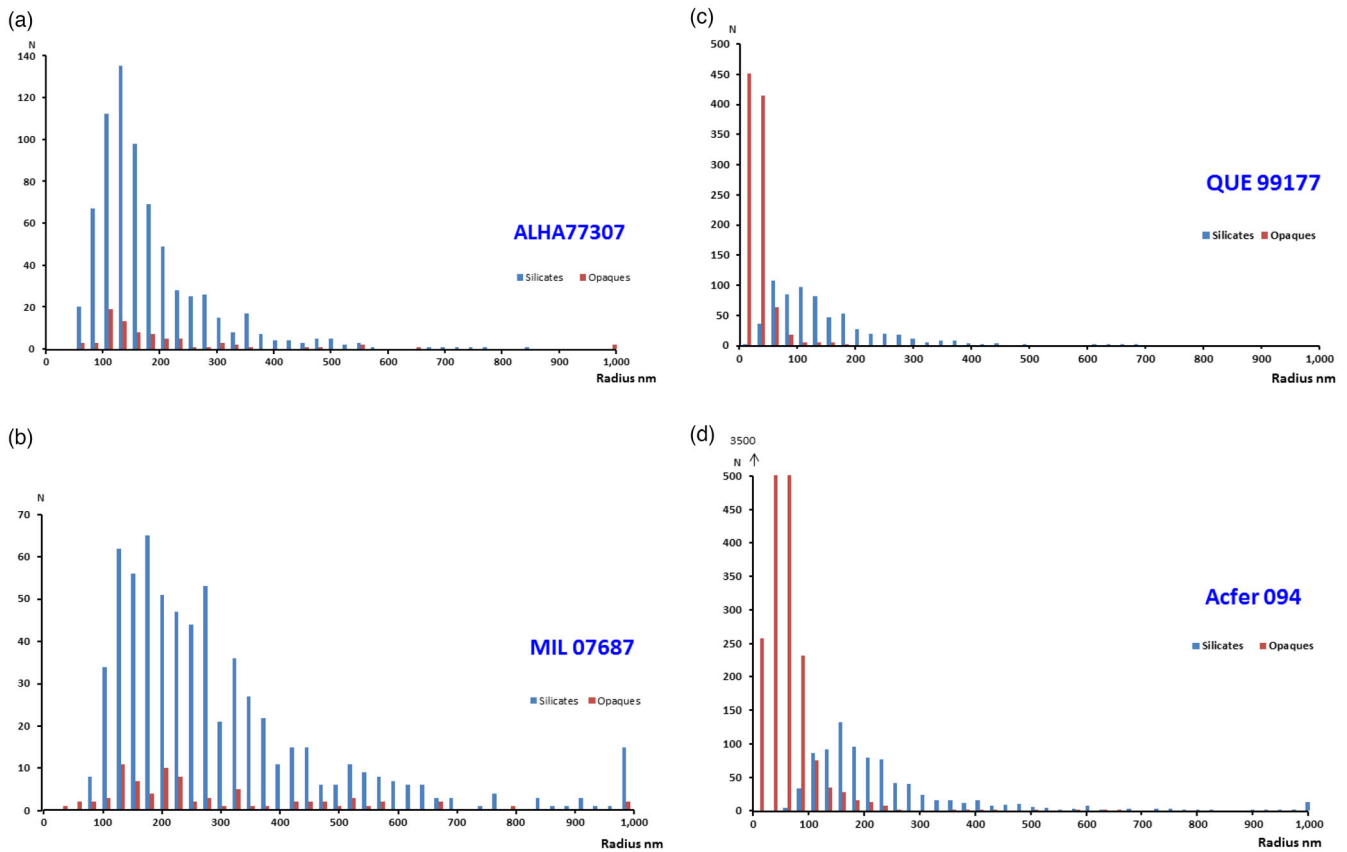
FIGURE 6. Histogram showing distribution of the radii for both the silicate and opaque phases for sample ALHA77307 (a), MIL 07687 (b), QUE 99177 (c), Acfer 094 (d).

The size of silicates was significantly higher than the size of opaque minerals. For QUE 99177, the mean radii were 103 nm ($+\sigma 18$, $-\sigma 16$) for silicates and 15 nm ($+\sigma 4$, $-\sigma 3$) for opaques, and for Acfer 094, the mean radii were 176 nm ($+\sigma 18$ $-\sigma 16$) for silicates and 26 nm ($+\sigma 6$, $-\sigma 5$) for opaques.

Figure 4 displays the geometric mean radii of silicate ($M_{\text{r-silicate}}$) grains plotted against that for the metal and metal–sulfide grains ($M_{\text{r-opaques}}$) in the samples of ALHA77307, MIL 07687, QUE 99177, Acfer 094. These are plotted together and compared with those values determined for CP-IDPs and comet 81P/Wild 2 in Wozniakiewicz et al. (2013).

The geometric mean radii of matrix grains display a similar range of values for $M_{\text{r-silicates}}$ and $M_{\text{r-opaques}}$ to the ones reported for cometary samples with a range of values extending to slightly smaller and larger values for opaque phases. However, while a clear trend line can be fitted to the cometary sample data, with $M_{\text{r-silicate}}$ being consistently larger than $M_{\text{r-sulfide}}$ in the ratio of their mean densities (0.62) as is expected for aerodynamic sorting, this is not the case for the meteorite matrix data. The meteorite matrix sample data sit on either side and far from the cometary trend line. Although a limited data set, it would appear that there are two groupings of meteorites matrix, each defining trend lines that are steeper (with $M_{\text{r-silicates}}$ being almost equal to $M_{\text{r-opaques}}$ in ALHA77307 and MIL07687) or shallower (with $M_{\text{r-silicates}}$ even larger than $M_{\text{r-opaques}}$ in QUE 99177 and Acfer 094) than that defined by the cometary samples (slope 0.62, Equation 5 below) potentially indicating the existence of two distinct populations. The slope of the trend lines in grain size supports aerodynamical sorting if it agrees with the density ratio of the grains (Wozniakiewicz et al., 2012, 2013). Here, however, the slope is not mineralogically meaningful.

The cumulative frequency distributions of silicate and metal and metal–sulfide grain sizes in the matrix of meteorites studied in this work are shown in Figure 5 and values of the geometric mean radii (Mr in nm) and standard deviations ($+\sigma$ and $-\sigma$ in nm) are reported in Table 1. Here, we see in more detail that the geometric mean radii of the grains (indicated by solid vertical lines) are similar for both silicate and sulfide grains in ALHA77307 and MIL 07687, but are markedly different, with that for silicates being much larger than for
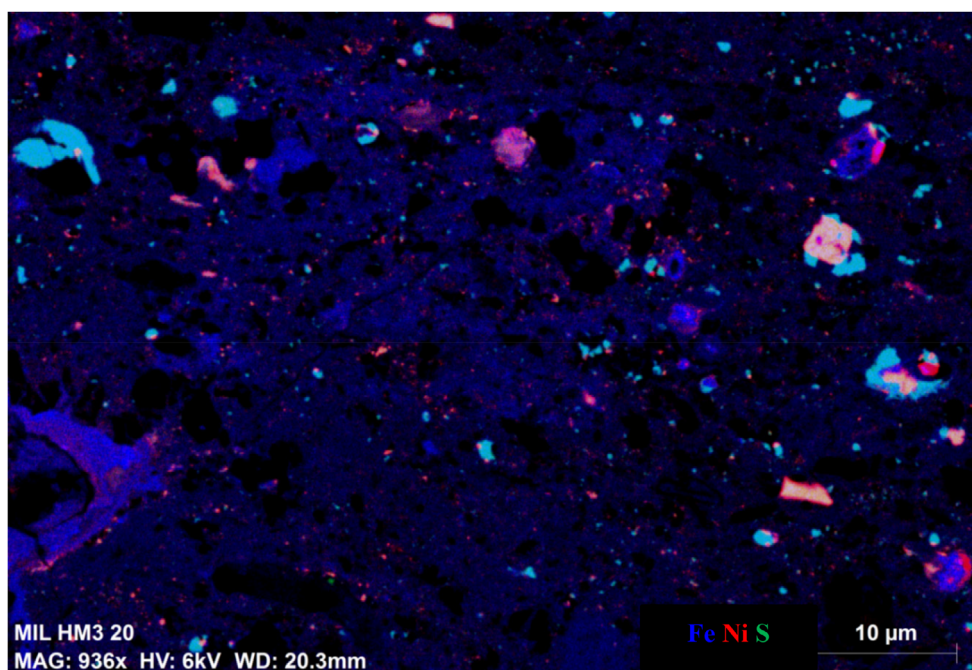
FIGURE 7. Element map of Acfer 094 Area 1 matrix acquired using the FEI Quanta with Fe = blue, Ni = red, S = green, showing the presence of nano-sized Ni-bearing phases (in red, pink, magenta), Fe-S phases (in Cyan), and metal (in blue) set in a groundmass also containing Fe.

opaques, in Acfer 094 and QUE 99177. Values of standard deviations about the mean values are indicated by shaded regions around each cumulative curve in Figure 5. For ALHA77307 and MIL 07687, the standard deviations for each meteorite overlap for both the silicate and sulfide size distributions. Thus, based on the grain sizes of each phase alone, the grain size distributions are not distinct, and the meteorites cannot be distinguished by them. In contrast, for Acfer 094 and QUE 99177, there is no overlap in standard deviation for either the opaques or silicates. Thus, the grain size distributions are distinct, and these two meteorites are distinguishable, from ALHA77307 and MIL 07687 by the mean radii of each phase. The grain size data are also plotted as histograms in Figure 6 to provide a better understanding of the underlying particle number density distributions. Here, the radii were binned into a series of consecutive, nonoverlapping intervals of 25 nm. Again, ALHA77307 and MIL 07687 exhibit similarities in the relative abundance of silicate versus opaque grains (ALHA77307: 709 silicates, 78 opaques—MIL07687: 662 silicates, 79 opaques, thus considerably more silicate grains measured in each), as well as the shape and location of their grain distribution, with the silicate and opaque distributions overlapping one another, but with a dramatic small size cutoff in the opaques in the 50–100 nm radius range in Figure 6a,b compared to the results in Figure 6c,d. The geometric means of Acfer 094 and QUE 99177 also show similarities, with both exhibiting much narrower distribution profiles for their opaque phases (Acfer 094: 840 silicates, 5007 opaques—QUE 99177: 647 silicates, 968 opaques). It is also evident that the data for the opaques are shifted toward smaller sizes compared to ALHA77307 and MIL 07687. This demonstrates that our sampling and analysis techniques are capable of detecting small opaque particles down to 10 nm radius and lends credibility to their observed absence in ALHA77307 and MIL 07687.

DISCUSSION

Aerodynamic Sorting and Comparison with IDPs

Wozniakiewicz et al. (2012) reported that when the geometric mean radii of silicate and sulfide grains in CP IDPs and comet 81P/Wild 2 are plotted against one another, a trend line can be fitted that satisfies the equation:

$$M_{\text{r-sulfide}} = 0.62 M_{\text{r-silicate}}. \qquad (5)$$

The slope of this trend line is approximately equal to the ratio of the average silicate to sulfide densities in these samples, suggesting the grains had been subjected to an aerodynamical size sorting mechanism prior to accretion. This is because a particle interacts with the
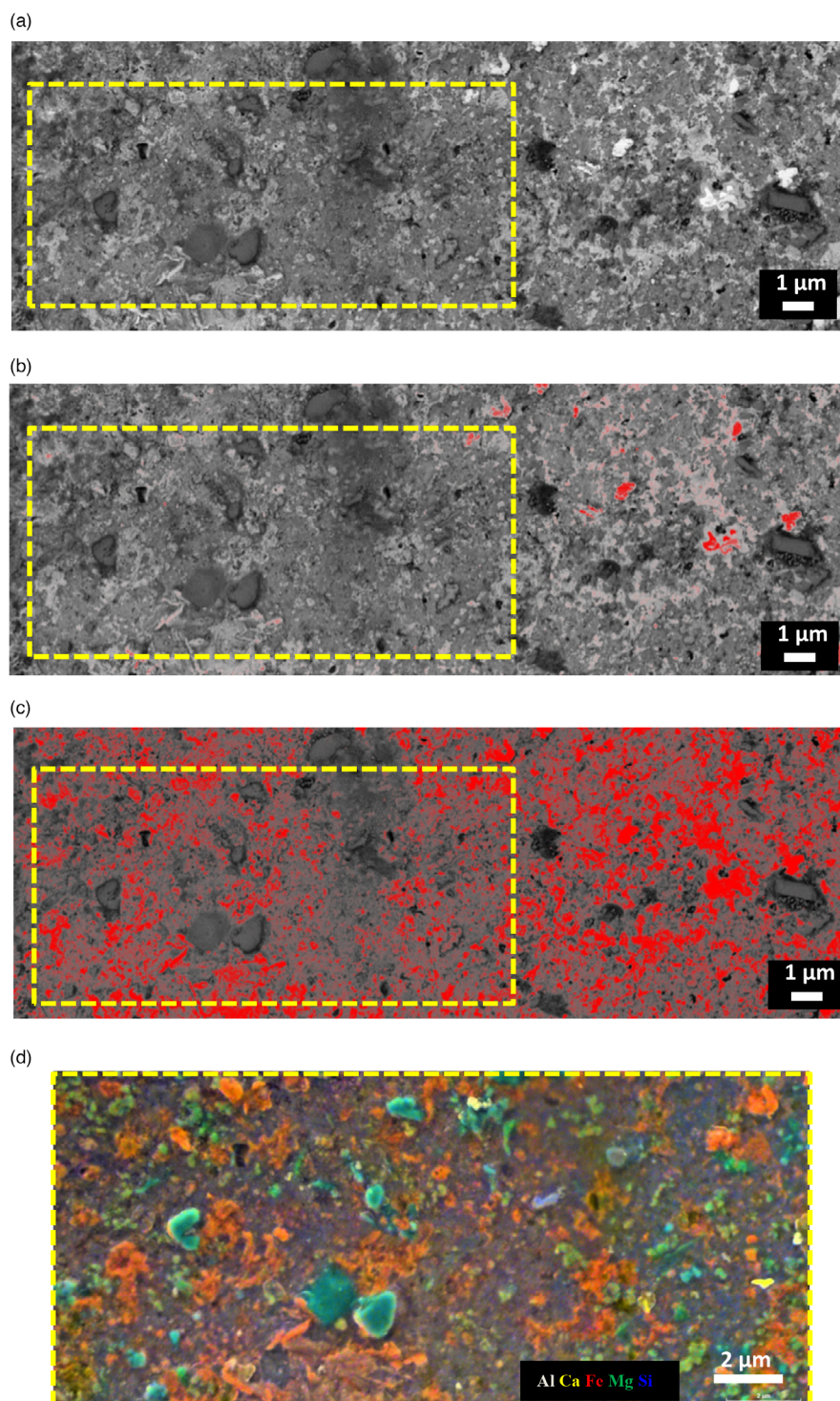
FIGURE 8. (a) Backscattered electron image of ALHA77307 Area 1 matrix acquired with the Zeiss Ultra Plus, showing the limited presence and relatively large size of opaque phases (brightest features). (b) Thresholding (in red) of the brightest phases, with brightness values ranging from 255 to 170, using Image J emphasizes the size and abundance of opaques. (c) Thresholding (in red) of the pale gray phase, with brightness values ranging from 169to 130, using Image J emphasizes the abundance of an Fe-rich phase that seems to be the product of alteration of the opaques. (d) Element map of ALHA77307 Area 1 matrix from the yellow-dashed box in (c) acquired with the FEI Quanta, showing the Fe-rich composition of the pale gray phase (in orange) in (a) (shown as red in c). Al = white, Ca = yellow, Fe = red, Mg = green, Si = blue. Mg-rich silicates (in green) set in an Si and Fe-rich groundmass (in purple) can also be seen.
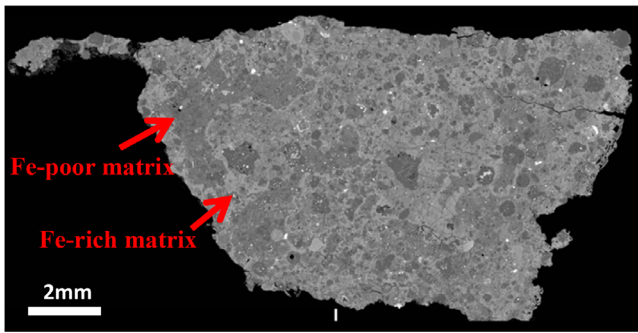
FIGURE 9. BSE image mosaic map of the entire section of sample MIL 07687 acquired using the Zeiss EVO SEM, showing the presence of Fe-rich (brighter) and Fe-poor (darker) matrix regions.

gas as determined by the product of its radius and density, so particles with the same radius–density product are aerodynamically equivalent.

The meteorite matrix samples reported here, in contrast, plot away from the cometary line (Equation 5).

The composition of matrix silicates is similar to those in CP IDPs and comet 81P/Wild 2, being compositionally similar to enstatite ($MgSiO_3$), forsterite (Mg_2SiO_4), with the additional presence of Fe-rich silicates in matrix of these meteorites, probably the result of the mild aqueous alteration experienced, and fragments of chondrules in the same meteorite. In contrast, the opaque components of the matrix are significantly different in overall composition to those studied in the cometary particles. This is due to the different method adopted; Wozniakiewicz et al. (2012, 2013) looked only at Fe-rich sulfides, which were mainly Ni-poor, whereas in this study, we looked at opaques which included metal sulfide (e.g., pyrrhotite, troilite pentlandite) and metal grains (e.g., Figure 7). Because of the difference in the type of opaque minerals being recorded, we do not expect the $M_{r\text{-opaques}}$ versus $M_{r\text{-silicates}}$ trend lines to be similar in the two studies. If the opaque components in the matrix of the meteorites were only represented by the presence of metal, then assuming densities of $7.8\,g\,cm^{-3}$, the ratio of densities becomes 0.41 (see gray trend lines in Figure 4) and Equation (5) can be rewritten as:

$$M_{r\text{-metal}} = 0.41 M_{r\text{-silicate}}. \qquad (6)$$

However, given that the matrix of the meteorites investigated here actually contains opaque phases that are a mixture of metal grains and Ni-bearing sulfides, the meteorite matrix samples should plot somewhere in between the two trend lines expressed by Equations (5) and (6) if the matrix grains have been subject to similar aerodynamic sorting prior to accretion. Given that none of the four meteorite matrix samples plot within the region defined by the two trend lines, it would appear that their size distributions are not primarily defined by pre-accretionary sorting. If the samples did undergo similar sorting, then another process or processes must have subsequently operated on the meteorite matrix materials.

Considering that aerodynamical sorting of submicron individual particles into aggregates is suggested by the results of Wozniakiewicz et al. (2012), the absence of the same sorting in chondrites could be diagnostic of a distinct process operating in the outer solar system. Indeed, one process that may be responsible for this sorting stems from the velocity dependence of collisions and consequent implications for preferred sticking when particle stopping times are comparable to the Kolmogorov eddy time (described in Pan & Padoan, 2014).

Evidence of Alteration

The meteorite parent bodies (asteroids) are generally believed to have experienced considerably higher degrees of heating and/or aqueous alteration than comets. After falling to the Earth, further terrestrial alteration may also have occurred that is not observed in the stratospheric and space collected cometary samples. Therefore, it is possible that any evidence of size sorting in the meteorite matrix may have been destroyed by such parent body processes or terrestrial weathering.

In an attempt to understand the difference between meteorite matrix with respect to opaques, the high-spatial resolution image maps were compared. These reveal that the matrix of samples ALHA77307 and MIL 07687 (where $M_{r\text{-silicates}} \approx M_{r\text{-opaques}}$) has experienced more pronounced aqueous alteration than QUE 99177 and Acfer 094 (where there is a more pronounced difference in $M_{r\text{-silicates}}$ and $M_{r\text{-opaques}}$). However, the style of aqueous alteration differs between ALHA77307 and MIL07687, for example, phyllosilicates are present in the matrix of ALHA77307 and ferrihydrite in MIL07687 which is rare in ALHA77307 (e.g., Brearley, 1993, 2012, 2013). The image map of the matrix of ALHA77307 (Figure 8b) shows few opaque grains (white phases in EsB images) and these are of relatively large size, with nano-sized (1–10 nm) opaque grains not visible, whereas nano-sized grains are clearly visible in Acfer 094 and QUE 99177 under the same data acquisition conditions. The matrix in ALHA77307 is also characterized by a high abundance of another moderately high Z (pale gray) phase (Figure 8b,c) which seems to be the product of alteration of the opaques. The element maps acquired show this to be an Fe, O-rich phase and is probably an iron oxide and/or an oxy-hydroxide, consistent with an origin as alteration of the opaque phase.
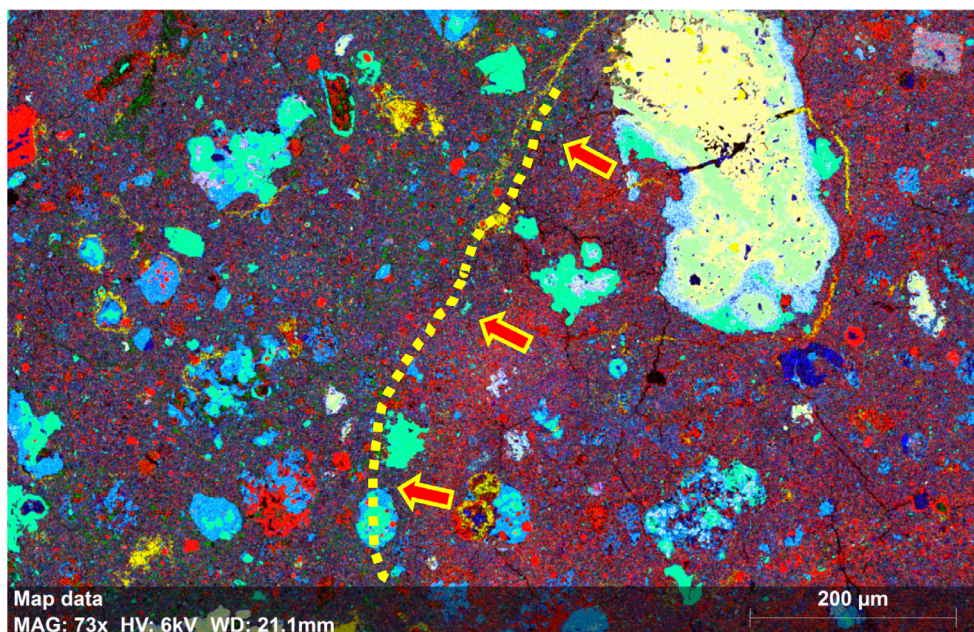
FIGURE 10. Element map of sample MIL 07687 acquired using FEI Quanta, showing a matrix region characterized by a clearly defined boundary (dashed yellow line) between the two different types of matrices, where the more Fe-rich matrix (prevalently in red) is abundant to the right of the yellow line. Al = white, Ca = yellow, Fe = red, Mg = green, Si = blue.

The matrix of the sample MIL 07687 also shows evidence of partial and localized aqueous alteration characterized by a fibrous FeO-rich phase that electron diffraction data suggest is ferrihydrite or akaganeite (Brearley, 2012). It is texturally complex and consists of highly irregular-shaped regions over a centimeter scale, with distinct contrast in EsB images (Figure 9). Brearley (2013) has shown that, at TEM scale, the FeO-rich regions advance and encompass the FeO-poor regions "dendritically" with a high abundance of randomly oriented fibrous phase. Based on the opaque grain morphology and the intimate association with the fibrous phases, Brearley (2013) suggested that the FeO-rich matrix appears to be the result of alteration of precursor matrix by a percolating Fe-rich fluid, from which the fibrous phase deposited. The FeO-poor regions of the matrix on the other hand represent the original, relatively unaltered matrix which escaped heavy aqueous alteration and appears now locally preserved. In the FeO-poor regions, opaque phases could be easily identified and counted on the element on the EsB montages acquired using the Zeiss Ultra Plus Field Emission SEM. The boundary between the two different types of matrices is clearly defined by the high concentration of Fe oxides outlining a very distinctive alteration front (Figure 10) implying that the availability of water was highly localized, and not evenly distributed throughout the rock (Brearley, 2013). As with ALHA77307, the EsB image maps of the matrix of MIL 07687 matrix (Figure 11a,b) also show a limited abundance of relatively large opaques (white phases in EsB images) and a lack of nano-sized opaque grains. The matrix in this sample is also characterized by the abundant presence of an Fe-rich phase, probably an iron oxide and/or an oxy-hydroxide (the moderately high Z, pale gray phase).

In QUE 99177 and Acfer 094, there is evidence of only minor alteration in their matrices. In contrast to ALHA77307 and MIL 07687, the matrices of QUE 99177 and Acfer 094 show a distinctive presence of abundant nano-sized opaque phases as shown in Figures 12 and 13.

The difference in size and abundance of opaque phases therefore appears to be possibly linked to the degree of aqueous alteration, with more pronounced aqueous alteration having attacked the nano-sized phases, dissolving them to produce the observed Fe-bearing oxide, or oxyhydroxide phases (and possibly Fe-bearing phyllosilicates), biasing the mean size of the opaques to much larger values, and shifting the position of those data sets above the cometary trend line on the $M_{\text{r-opaques}}$ versus $M_{\text{r-silicates}}$ plot. Indeed, the size of sulfides appears to be a remarkably sensitive indicator of alteration, and this could potentially be quantified in the future to calibrate small degrees of aqueous alteration.

The samples for this work were selected based on their pristine nature, as indicated by the presence of amorphous silicates and high abundance of presolar grains in the matrix (e.g., Davidson et al., 2014; Hopp & Vollmer, 2018; Ohtaki et al., 2021; Ong & Floss, 2015; Nguyen et al., 2010; Vollmer et al., 2020). However, it is clear that they did not entirely escape aqueous alteration.
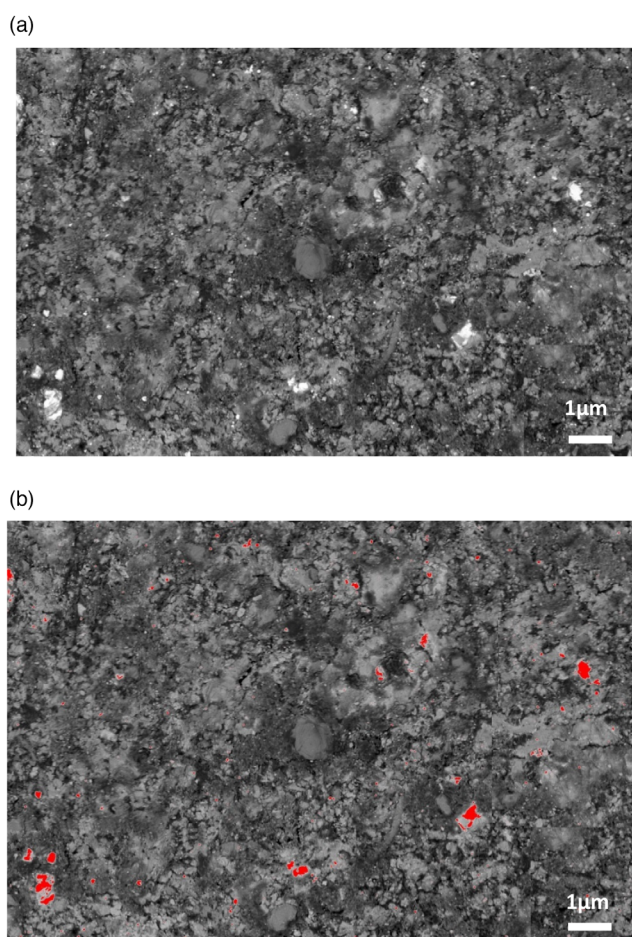
FIGURE 11. (a) Matrix EsB image montage of MIL 07687 Area 1 acquired with the Ultra Plus, showing evidence for aqueous alteration and limited presence and relatively large size of opaque phases. (b) Thresholding of the white phases (225–165 brightness range) of same area using Image J emphasizing the size and abundance of opaques.

Since the matrix is porous, easily allowing fluid percolation, it is particularly susceptible to alteration and its effects can be observed even in meteorites regarded as the most pristine like Acfer 094. In addition to that, aqueous alteration and terrestrial weathering have affected different meteorites to different degrees, and the effects of these processes are reflected in the results of this study. Whether the alteration occurred in an asteroid or on Earth, its consequence on the matrix grain size distribution may be the erasure of any evidence for size sorting.

Comparing Acfer 094 Size Distribution Data to Literature Data

Greshake (1997) investigated the mineralogical and chemical characteristics of the fine-grained matrix of the unique primitive carbonaceous chondrite Acfer 094 by scanning electron microscopy (SEM) and analytical transmission electron microscopy (ATEM). The grain size results reported by Greshake (1997) for the sample Acfer 094 are compared to grain size distributions determined from this study. The histogram in Figure 14a,b shows that there is a clear agreement with the data reported for the silicates in terms of sizes, yet there is a discrepancy between the data from this study, and that from Greshake (1997) in terms of sizes and abundances of the opaque phases. We found that, in contrast to what Greshake reported, the most abundant minerals, by number, in the matrix are opaques rather than olivines with 840 silicate grains versus 5007 opaque grains measured. In our study, we observed abundant opaque phases ≤50 nm in radius that were not reported by Greshake (1997). This is likely due to differences in analytical capabilities. Our new-generation SEMs are able to detect grain sizes smaller than was possible previously. In addition, by introducing multiple maps at different spatial resolutions across the section, our maps show how unevenly the nano-sized phases are distributed throughout the matrix. Cutting out FIB foils from regions of the matrix that are underpopulated by these nano-phases for ATEM investigations could lead to an inaccurate estimation of the size and abundances of the mineralogical phases present in the matrix. This reinforces the advantages of using high-spatial resolution SEM images and element maps which sample larger regions of the matrix, for samples in which grain sizes are sufficiently large, compared to the small cross sections investigated using TEM foils.

SUMMARY AND CONCLUSIONS

Pre-accretional processes operating in the protoplanetary disk, such as disk winds and nebula turbulence, affect the dynamics of dust grains, possibly causing their size sorting (Miyake et al., 2016).

While previous studies have shown that CP-IDP particle size distributions are compatible with aerodynamic sorting prior to accretion, matrix constituents (silicates and opaques) of chondritic meteorites investigated here do not show such trends.

The origin of nano-sized phases is not clearly understood, and it has been proposed that the most plausible formation mechanism is annealing of an amorphous precursor either in the solar nebula or in the parent body (Abreu & Brearley, 2010). If nano-sized phases have separated out from the amorphous silicates, and so never been dissociated as discrete grains, the disk winds and turbulence in the protoplanetary disk could not have produced a sorting effect when bringing them into the chondrite-forming region.

The general lack of sorting evidence might indicate that the smaller grains in carbonaceous chondrite matrix
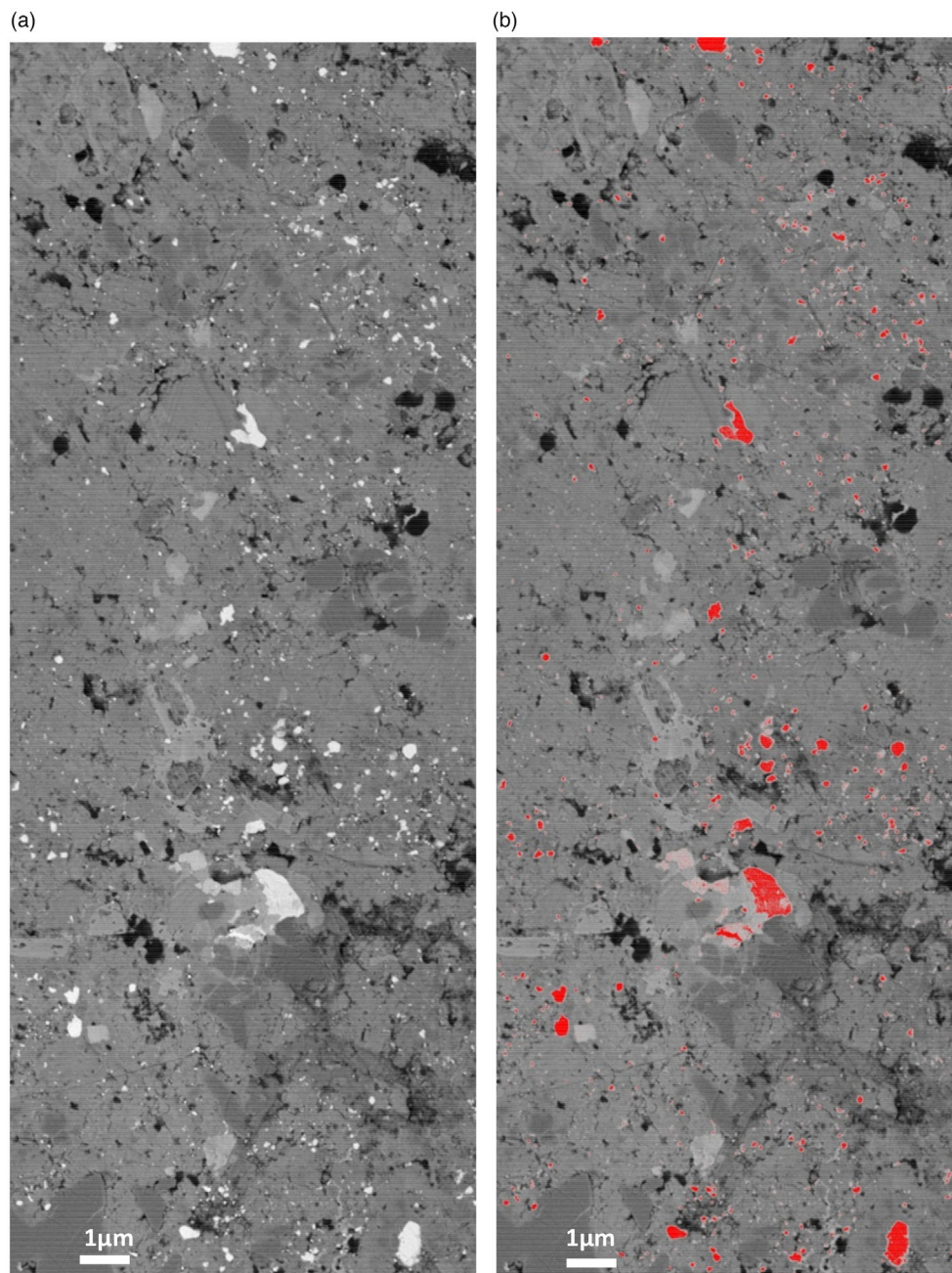
FIGURE 12. (a) EsB image montage of QUE 99177 Area 2 acquired with the Ultra Plus, showing the presence of opaque phases with a wider range of grain sizes. (b) Thresholding of the white phases (225–165 brightness range) of same area using Image J emphasizing the different size and abundance of opaque phases.

were not subject to sorting, unlike chondrule-sized aggregates that were affected by size sorting (Simon et al., 2018; Teitler et al., 2010). This could be diagnostic of the different environment in which chondrites and CP-IDPs aggregates formed and, in fact, evidence of a process occurring only in the outermost solar system which should be investigated further.

Alternatively, overprinting by terrestrial weathering and parent body processes, such as aqueous alteration and/or mild thermal metamorphism, may have destroyed this evidence by causing grain coarsening or metasomatic transformations. The size of the metal and metal–sulfides occurring in the matrix of the samples investigated in this study appears to be controlled predominantly by
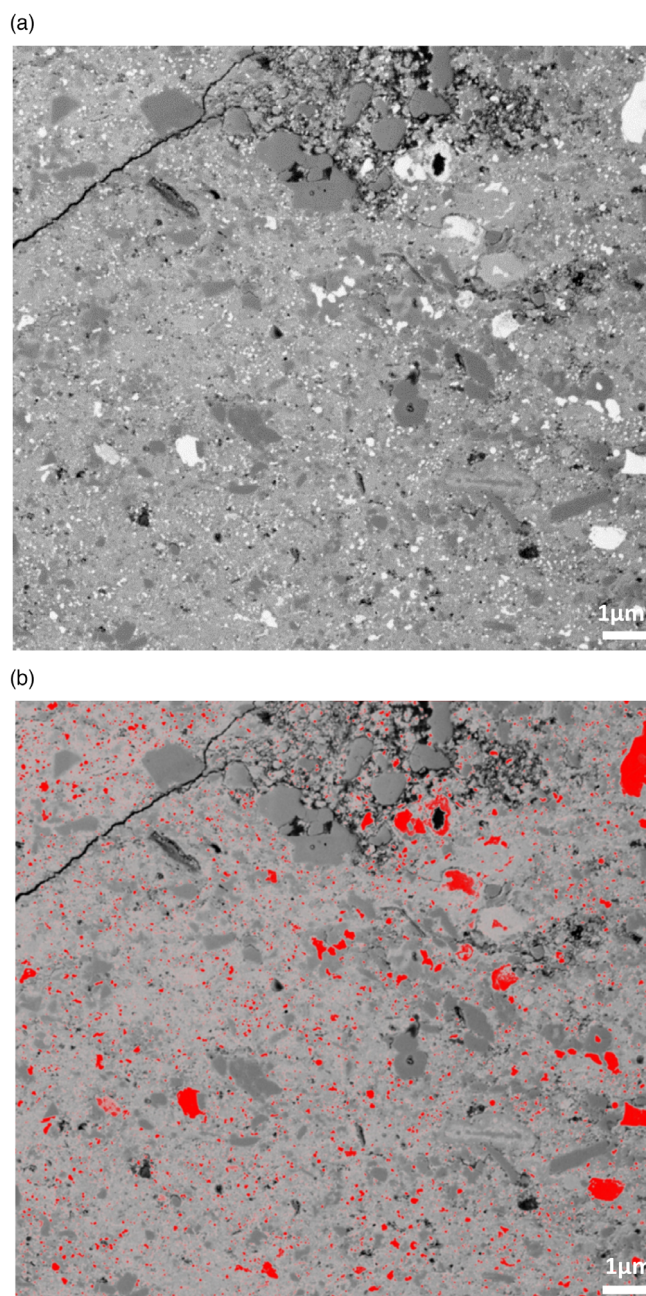
(a)

(b)

FIGURE 13. (a) EsB image montage of Acfer 094 Area 1 acquired with the Ultra Plus, showing the presence of opaque phases with a wider range of grain sizes. (b) Thresholding of the white phases (225-165 brightness range) of same area using Image J emphasizing the different size and abundance of opaque phases.

(a)

(b)

FIGURE 14. Histogram showing distribution of the radii for the (a) silicate phases in Acfer 094 and (b) opaque phases in Acfer 094.

post-accretionary processes and was probably not determined by aerodynamical processes such as in IDPs.

Based on SEM observations, it appears evident that nano-sized phases are very sensitive to alteration and indeed may be considered the most sensitive indication of
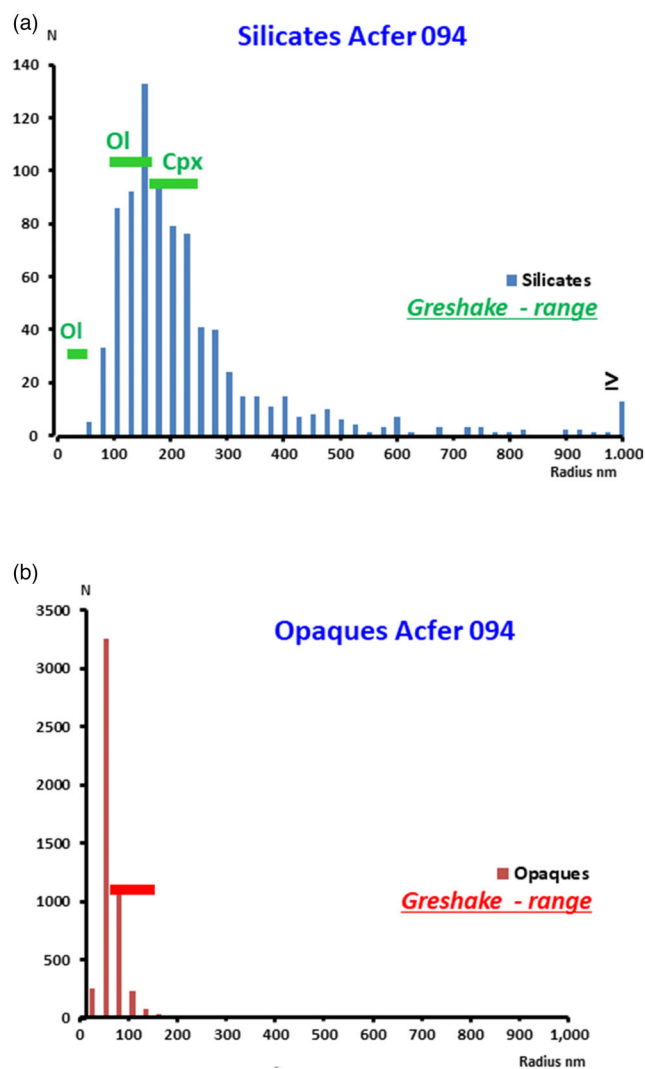
alteration. These properties could be exploited in future work to quantify parent body processing.

This study has also highlighted the importance of investigating wide surface areas by SEM rather than relying solely on FIB sections, reinforcing the importance of the use of both techniques in coordinated studies. Given the extremely high heterogeneity of the matrix, and the nonuniform distribution in abundance of mineral phases, it is crucial to contextualize the observations to ensure the misrepresentation of mineral phase abundances is minimized. A combined SEM and TEM analysis of meteorite matrix grain sizes is recommended for future studies.

REFERENCES

Abreu, N. M., and Brearley, A. J. 2010. Early Solar System Processes Recorded in the Matrices of Two Highly Pristine CR3 Carbonaceous Chondrites, MET 00426 and QUE 99177. *Geochimica et Cosmochimica Acta* 74: 1146–71.

Blott, S. J., and Pye, K. 2001. Gradistat: A Grain Size Distribution and Statistics Package for the Analysis of Unconsolidated Sediments. *Earth Surface Processes and Landforms* 26: 1237–48.

Bradley, J. P. 1999. An Infrared Spectral Match Between GEMS and Interstellar Grains. *Science* 285: 1716–8.

Bradley, J. P. 2013. How and Where did GEMS Form? *Geochimica et Cosmochimica Acta* 107: 336–40.

Brearley, A. J. 1993. Matrix and Fine-Grained Rims in the Unequilibrated CO3 Chondrite, ALHA77307: Origins and Evidence for Diverse, Primitive Nebular Dust Components. *Geochimica et Cosmochimica Acta* 57: 1521–50.

Brearley, A. J. 2012. MIL 07687—An Intriguing, Very Low Petrologic Type 3 Carbonaceous Chondrite with a Unique Style of Aqueous Alteration. 43rd Lunar and Planetary Science Conference, abstract #1233.

Brearley, A. J. 2013. Miller Range Mil07687: A Unique Carbonaceous Chondrite with a Complex Record of Partial Aqueous Alteration. 76th Annual Meteoritical Society Meeting. p. 5206.

Brownlee, D. E., and Joswiak, D. J. 1995. Identification of Cometary and Asteroidal Particles in Stratospheric IDP Collections. 24th Lunar and Planetary Science Conference, abstract #1092.

Brownlee, D. E., Joswiak, D. J., Love, S. G., Nier, A. O., Schlutter, D. J., and Bradley, J. P. 1993. Identification of Cometary and Asteroidal Particles in Stratospheric IDP Collections. 24th Lunar and Planetary Science Conference, abstract #1452.

Busemann, H., Nguyen, A. N., Cody, G. D., Hoppe, P., Kilcoyne, A. L. D., Stroud, R. M., Zega, T. J., and Nittler, L. R. 2009. Ultra-Primitive Interplanetary Dust Particles from the Comet 26P/Grigg–Skjellerup Dust Stream Collection. *Earth and Planetary Science Letters* 288: 44–57.

Clayton, D. 1980. Chemical and Isotopic Fractionation by Grain Size Separates. *Earth and Planetary Science Letters* 47: 199–210.

Cuzzi, J. N., Hogan, R. C., Paque, J. M., and Dobrovolskis, A. R. 2001. Size-Selective Concentration of Chondrules and Other Small Particles in Protoplanetary Nebula Turbulence. *Astrophysics Journal* 546: 496–508.

Cuzzi, J. N., Hogan, R. C., and Shariff, K. 2008. Toward Planetesimals: Dense Chondrule Clumps in the Protoplanetary Nebula. *Astrophysics Journal* 687: 1432–47.

Cuzzi, J. N., Hartlep, T., Simon, J. I., and Estrada, P. R. 2017. Planetesimals Born Big by Clustering Instability? Accretion: Building New Worlds Conference. p. 2039.

Davidson, J., Busemann, H., and Franchi, I. A. 2012. A NanoSIMS and Raman Spectroscopic Comparison of Interplanetary Dust Particles from Comet Grigg-Skjellerup and Non-Grigg Skjellerup Collections. *Meteoritics & Planetary Science* 47: 1748–71.

Davidson, J., Nittler, L. R., Alexander, C. M. O'D., and Stroud, R. M. 2014. Presolar Materials and Nitrogen Isotope Anomalies in the Unique Carbonaceous Chondrite Miller Range 07687. 45th Lunar and Planetary Science Conference, abstract #1376.

Folk, R. L., and Ward, W. C. 1957. A Study in the Significance of Grain-Size Parameters. *Journal of Sedimentary Petrology* 3: 27.

Friedman, G. M. 1958. Determination of Sieve-Size Distribution from Thin-Section Data for Sedimentary Petrological Studies. *The Journal of Geology* 66: 4–416.

Greshake, A. 1997. The Primitive Matrix Components of the Unique Carbonaceous Chondrite Acfer 094: A TEM Study. *Geochimica et Cosmochimica Acta.* 61: 437–52.

Hartlep, T., and Cuzzi, J. N. 2020. Cascade Model for Planetesimal Formation by Turbulent Clustering. *Astrophysics Journal* 892: 2020.

Hartlep, T., Cuzzi, J. N., and Weston, B. 2017. Scale Dependence of Multiplier Distributions for Particle Concentration, Enstrophy, and Dissipation in the Inertial Range of Homogeneous Turbulence. *Physical Review E* 95: 033115.

Hopp, T., and Vollmer, C. 2018. Chemical Composition and Iron Oxidation State of Amorphous Matrix Silicates in the Carbonaceous Chondrite Acfer 094. *Meteoritics & Planetary Science* 53: 153–66.

Kuebler, K. E., McSween, H. Y., Jr., Carlson, W. D., and Hirsch, D. 1999. Sizes and Masses of Chondrules and Metal–Troilite Grains in Ordinary Chondrites: Possible Implications for Nebular Sorting. *Icarus* 96: 141.

Le Guillou, C., Dohmen, R., Rogalla, D., Müller, T., Vollmer, C., and Becker, H.-W. 2015. New Experimental Approach to Study Aqueous Alteration of Amorphous Silicates at Low Reaction Rates. *Chemical Geology* 412: 179–92.

Liffman, K. 2005. Chondrule and Metal Grain Size Sorting from Jet Flows. *Meteoritics & Planetary Science* 40: 123–38.

Messenger, S. 2000. Identification of Molecular-Cloud Material in Interplanetary Dust Particles. *Nature* 404: 968–71.

Miyake, T., Suzuki, T. K., and Inutsuka, S. 2016. Dust Dynamics in Protoplanetary Disk Winds Driven by Magnetorotational Turbulence: A Mechanism for Floating Dust Grains with Characteristic Sizes. *Astrophysics Journal* 821: 3.

Molster, F. J., and Waters, L. B. F. M. 2003. The Mineralogy of Interstellar and Circumstellar Dust. *Astromineralogy* 609: 121–70.

Nguyen, A. N., Nittler, L. R., Stadermann, F. J., Stroud, R. M., and Alexander, C. M. O'D. 2010. Coordinated Analyses of Presolar Grains in the Allan Hills 77307 and Queen Elizabeth Range 99177 Meteorites. *Astrophysics* 719: 166–89.

Nguyen, A. N., Stadermann, F. J., Zinner, E., Stroud, R. M., Alexander, C. M. O'D., and Nittler, L. R. 2007. Characterization of Presolar Silicate and Oxide Grains in Primitive Carbonaceous Chondrites. *Astrophysics Journal* 656: 1223–40.

Ohtaki, K. K., Ishii, H. A., Bradley, J. P., Villalon Kr, L., Davis, A. M., Stephan, T., Bustill, K. C., and Ciston, J. 2021. Search for Meteoritic GEMS I: Comparison of Amorphous Silicates in Paris and Acfer 094 Chondrite Matrices and in Anhydrous Chondritic Interplanetary Dust Particles. *Geochimica et Cosmochimica Acta.* 310: 321–45.

Ong, W. J., and Floss, C. 2015. Iron Isotopic Measurements in Presolar Silicate and Oxide Grains from the Acfer 094 Ungrouped Carbonaceous Chondrite. *Meteoritics & Planetary Science* 50: 1392–407.

Pan, L., and Padoan, P. 2014. Turbulence-Induced Relative Velocity of Dust Particles. The Bidisperse Case. *Astrophysics Journal* 791: 48.

Poteet, C. A., Megeath, S. T., Watson, D. M., Calvet, N., Remming, I. S., McClure, M. K., Sargent, B. A., et al. 2011. A Spitzer Infrared Spectrograph Detection of Crystalline Silicates in a Protostellar Envelope. *Astrophysics Journal* 733: 32.

Rubin, A. E., and Keil, K. 1984. Size-Distributions of Chondrule Types in the Inman and Allan Hills A77011 L3 Chondrites. *Meteoritics* 19: 135.

Sandford, S. A., and Walker, R. M. 1985. Laboratory Infrared Transmission Spectra of Individual Interplanetary Dust Particles from 2.5 to 25 Microns. *Astrophysical Journal* 291: 838–51.

Shu, F. H., Shang, H., Glassgold, A. E., and Lee, T. 1997. X-Rays and Fluctuating X-Winds from Protostars. *Science* 277: 1475–9.

Simon, J. I., Cuzzi, J. N., McCain, K. A., Cato, M. J., Christoffersen, P. A., Fisher, K. R., Srinivasan, P., Tait, A. W., Olson, D., and Scargle, J. D. 2018. Particle Size Distributions in Chondritic Meteorites: Evidence for Pre-Planetesimal Histories. *Earth and Planetary Science Letters* 494: 69–82.

Skinner, W. R., and Leenhouts, J. M. 1993. Size Distributions and Aerodynamic Equivalence of Metal Chondrules and Silicate Chondrules in ACFER 059. 24th Lunar and Planetary Science Conference, abstract #1659.

Teitler, S. A., Paque, J. M., Cuzzi, J. N., and Hogan, R. C. 2010. Statistical Tests of Chondrule Sorting. *Meteoritics & Planetary Science* 45: 1124–35.

Van Boekel, R., Waters, L. B. F. M., Dominik, C., Dullemond, C. P., Tielens, A. G. G. M., and de Koter, A. 2004. Spatially and Spectrally Resolved 10 μm Emission in Herbig Ae/Be Stars. *Astronomy & Astrophysics* 418: 177–84.

Verniani, F. 1969. Structure and Fragmentation of Meteoroids. *Space Science Reviews* 10: 230–61.

Vollmer, C., Leitner, J., Kepaptsoglou, D., Ramasse, Q. M., King, A. J., Schofield, P. F., Bischoff, A., Araki, T., and Hoppe, P. 2020. A Primordial 15N-Depleted Organic Component Detected within the Carbonaceous Chondrite Maribo. *Nature* 10: 20251.

Watson, D. M., Leisenring, J. M., Furlan, E., Bohac, C. J., Sargent, B., Forrest, W. J., Calvet, N., Hartmann, L., Nordhaus, J. T., and Green, J. D. 2009. Crystalline Silicates and Dust Processing in the Protoplanetary Disks of the Taurus Young Cluster. *Astrophysics Journal Supplement* 180: 84.

Wozniakiewicz, P. J., Bradley, J. P., Ishii, H. A., Brownlee, D. E., Kearsley, A. T., Burchell, M. J., and Price, M. C. 2012. Grain Sorting in Cometary Dust from the Outer Solar Nebula. *Astrophysics Journal* 60: L23.

Wozniakiewicz, P. J., Bradley, J. P., Ishii, H. A., Price, M. C., and Brownlee, D. E. 2013. Pre-Accretional Sorting of Grains in the Outer Solar Nebula. *Astrophysics Journal* 779: 164.